2011

Simulation of cell seeding and retention in a disordered polymeric scaffold

Tejaswini Narayana
Louisiana State University and Agricultural and Mechanical College, tnaray1@lsu.edu

SIMULATION OF CELL SEEDING AND RETENTION IN A DISORDERED POLYMERIC SCAFFOLD

A Thesis

Submitted to the Graduate Faculty of the
Louisiana State University and
Agricultural and Mechanical College
in partial fulfillment of the
requirements for the degree of
Master of Science in Chemical Engineering

in

The Gordon A. and Mary Cain Department of Chemical Engineering

by
Tejaswini Narayana
Bachelor of Technology, University of Kerala, 2005
December 2010

Dedicated to

My parents

ACKNOWLEDGEMENTS

I thank my advisors Dr. Karsten. E Thompson and Dr. James. E Henry for their guidance which made this work possible. I thank Dr. Martin H. Hjortso for taking out time to be on my committee.

I thank Dr. Kyungmin Ham for the XMCT imaging of my sample. I thank Pradeep Bhattad for cleaning and segmentation of the XMCT image of my sample and Nathan Lane for providing the FEM code for solving Stokes Equation. I thank my labmates Pradeep Bhattad, Nathan Lane, Amin Mirsaeidi, Qiang Sheng, Yijie Shen and Saade Bou-Mikael for all their help. I thank Ryan Al-Marhoun for his work in visualizing my data. I appreciate Imtiaz Hossain for his help in the visualization.

I thank the Gordon A. and Mary Cain Department of Chemical Engineering for my assistantship and the Engineering Sciences for providing funds to support this research. I thank the Center for Advanced Microstructures and Devices (CAMD), LSU for enabling the imaging required for my work and Louisiana Optical Initiative (LONI) for providing the HPC infrastructure required to run my simulation. I thank the LSU staff for their assistance. My thanks to the Middleton Library for good fiction that kept me entertained.

I thank my classmates Khue Nyugen, Edgardo Kamar, Gregory Robertson and Imran Chiragh for their help. I thank Anuja Ghosh, Purnima Narayanan, Nawsheen Golamhossen, Akanksha V. Kanitkar, Monika Gadre and Shrinidhi Shetty for keeping me sane. I thank Dr. Jyothi U. Rao, Nachal Devi Subramanian, Thilanga Liyana Arachchi, Misagh Naderi, Bamidele Adediji, Ali Ghamsari, Helbert Arenas, Mauricio Toscano, Belen Toscano, and Maria Toscano for their company.

I thank my friends Anushreedha S.S and Anu Rachel Jogi for always being there for me. I thank all my friends for their support.

I thank my partner Pratap Bhat for his love and support and “the happy ending” to my journey so far.

I express my love and gratitude to my parents, Mrs. Chandrakala Delampady and Dr. Narayana Delampady and brother Tapan Narayana for their love and encouragement, and their faith in me.

TABLE OF CONTENTS

LIST OF FIGURES

LIST OF SYMBOLS

a	radius of the particle
d	distance between the particle and the pore surface
D	Diffusion coefficient
Pe	Peclet number
$\mathbf{u}$	Velocity
δ_M	Uniform characteristic displacement length
Δt	Time step
Δr	Displacement in a time step
$\boldsymbol{\xi}$	Random Gaussian variable
$\boldsymbol{\upsilon}$	Velocity due to viscous resistance

ABSTRACT

Historically, bone repair has been performed using materials like metals, ceramics, cements and bioactive glass. The major problem with all these materials is that they do not perform the necessary non-structural functions of bone. Engineered tissue, created by growing bone cells on porous biodegradable material (scaffold), will address this issue with current bone repair techniques.

Improving engineered tissue treatments requires a thorough understanding of factors affecting cell seeding and proliferation inside a disordered porous material which is not feasible using current experimental techniques. A model for particle transport in a disordered porous material that can predict the particle deposition pattern will be useful to understand the factors influencing particle transport and retention. Such a model has applications ranging from biomedical, microfluidics, environmental and water treatment. Currently available models for filtration or contaminant transport in a porous media either consider the porous media to be uniform or do not predict the particle deposition pattern. We develop an image-based computational model, which incorporates the structure of a disordered porous material, to study the effect of flow and material internal structure on particle transport and deposition, which was then applied to cell seeding. Particle motion and attachment inside the porous material is controlled by a deterministic convection component, obtained by numerically solving the Stokes Equation using FEM; a stochastic diffusion component, modeled using a random walk process, and an electrostatic component estimated using analytical expressions for the interaction of a colloid particle with a surface.

Our simulations show that the Peclet number has a significant effect on the cell attachment pattern in a scaffold. At low Peclet numbers, cell attachment is concentrated at the inlet region of

the scaffold, while cells penetrate deeper into the scaffold with increasing Peclet number. Additionally, the seeding pattern is found to vary considerably with internal pore structure. Visualization of the data indicates that attachment clusters at low velocity diffusion dominated zones.

CHAPTER 1 INTRODUCTION

1.1 Motivation

A model to track particles flowing through a porous media in a Stokes flow regime (creeping flow) has applications in biomedical, microfluidics, environmental and water treatment. A particularly important application of this research would be to help design treatments for bone defects using degradable polymeric scaffolds seeded with healthy bone cells. One of the current problems with using scaffolds in tissue regeneration is the rapid formation of tissue on the outer edge of the scaffold while the cells at the center become necrotic. Research in developing scaffolds with channels at the centre has been investigated to address this problem with some success in improving nutrient and cell transfer to the scaffold center. Comparisons between a series of scaffolds with channel diameters ranging from 170 to 421 μm have shown that cell coverage is linearly proportional to channel diameter and that no cell coverage is found within the scaffold for pore sizes below 82 μm (Rose et al. 2004).

Material geometry, degradation rate, flow pattern at site of insertion etc. play a major role determining the optimal seeding pattern. Some of the previous experimental works in this area have shown that starting with a scaffold having a uniform cell distribution ultimately resulted in a more uniform tissue (Freed et al. 1998; Holy et al. 2000; Ishaug-Riley et al. 1998; Kim et al. 1998; Martin et al. 2004). Achieving uniform tissue depends on many factors, including cellular ingrowth, cell adhesion (Palecek et al. 1997), effective transport of nutrients and oxygen into the scaffold and waste and carbon dioxide out of the scaffold (Botchwey et al. 2003).

In addition to bulk material design, modeling would give us an insight into microscopic behavior of the scaffold and allow us to pinpoint “failure sites” that are attributed to transport issues. Developing a reliable model to predict the pattern of cell movement and attachment

within a porous material allows prescreening and selection of the most viable materials, dramatically decreasing experimental time and cost. This can speed up the process of launching a polymeric scaffold in the market.

1.2 Objective

This research has been conducted to develop an image-based model for micro- and nano-particle transport in disordered porous media. We expect that it will be used to further understand the relationships between the internal architecture of a porous material, the flow properties in the medium, and particle transport to likely sites of deposition in the porous media. It could be applied to the study of cell seeding in a porous tissue scaffold. The detailed objectives of this work are to:

1. Develop a model for colloid transport and deposition that incorporates the real internal structure of a disordered porous material.

2. Apply the model to a preliminary study of a cell transport in a tissue scaffold, relating the scaffold internal structure and flow properties on the likely attachment pattern of bone cells.

To meet these objectives, research was conducted as follows.

1. Use of X-ray micro computed tomography (XMCT) to generate an image of a real porous material prepared using a technique that is currently accepted for the manufacture of polymeric scaffolds for clinical applications.

2. Divide the pore space into a set of non-overlapping tetrahedral elements; compute the velocity at each point in the pore space by solving the Stokes flow equations using Finite Element Method (FEM).

3. Calculate the particle position at varying time steps based on the different forces acting in the system.

4. Note the position and local conditions for particle attachment.

CHAPTER 2 BACKGROUND AND LITERATURE REVIEW

2.1 Background

2.1.1 Particle Transport in Porous Media

Colloid particle transport in porous media has been studied by researchers working in the field of groundwater contamination as there is evidence that contaminants adhere onto colloid particles and spread in a porous media due to the motion of the colloid particle (Mills et.al 1990). This problem is also important in understanding deep bed filtration (DBF) which is critical to control for the success of water flooding operations for enhanced oil recovery (Rege and Fogler 1988). Of these studies, most of the computational work treats the porous media as a packing with grains (collectors) of the same size and space between the grains to be uniform, which is not realistic for real porous materials. We include computational work on particle transport that incorporates some of the properties of the porous media in this section.

Rege and Fogler (1988) develop a network model to simulate the flow of emulsions and solid particles through porous media. This model has been designed to predict effluent concentration profiles, permeability changes occurring during deep bed filtration, and the evolution of the filter coefficient with time. Network models consist of junctions (nodes) and channels (bonds). In their work, pore size distribution of the porous material sample is obtained by mercury porosimetry. Many networks are generated by randomly distributing the pore size distribution to the bond lengths in the network. Simulation is performed on all these networks and the calculated values of the terms of interest are averaged and reported. The fluid flow distribution within the network is calculated by simultaneously solving mass balance equations for the fluid at every node. At every node the path taken by the particle (out of a choice of the several paths) is determined by

flow-biased probability, which biases the movement of the particle toward the path with greater flow. Particle deposition can occur in two ways. Straining occurs when the particle diameter is greater than the bond diameter. Another possibility is direct interception (i.e. deposition of a particle on a pore wall (bond) in the network). This event depends on the value of a lumped parameter θ that takes into account fluid velocity, ionic strength, pH, fluid properties, and particle density and concentration. Conditions favoring greater deposition result in higher values of θ. The filter coefficient, defined as the ratio of the volume of particles captured in a small volume element of the network to the volume of particles entering that element, is determined by the model.

Since it is not possible to determine the location of every deposited particle within a bond, Rege and Fogler's model cannot give a spatial distribution of particle deposition sites within the porous media. Another problem with this model is that it does not incorporate the actual internal pore structure of a real porous material as network models are approximations based on the real structure. Finally, in the network model approach, particles cannot follow a single streamline through nodal junctions, which prevents the simulation of high-Peclet-number transport.

Long et al (2010) perform pore-scale simulations of particle flow and transport through a filter to predict clean-bed filtration of nanoparticles from a 3D image of a filter. The filter is a packing of equal sized uniform flattened spheres. High-resolution volumetric images of the filtration column are obtained by using non-destructive microfocus X-ray computed tomography (MXCT) system. The Navier Stokes equations are solved numerically using Lattice Boltzmann method and velocity profile in the pore space is obtained. Concentration profiles of nanoparticles in the pore space are obtained by solving the advection-diffusion equation. This model assumes there are no deposited particles in the porous media. This model is only valid for filters in their initial stage of operation. As filtration proceeds accumulation of deposited particles increases

with time which has a significant effect on the filtration process. The model does not recompute the velocity profile to account for a change in the internal structure of the porous material with time as a result of particle deposition. This model determines the average collector efficiency which is a bulk property of the filter (porous media). This model does not give the particle deposition pattern in the filter at the end of the filtration process.

2.1.2 Bone Repair

Bone loss can occur due to infection, loss of blood supply, immobilization, fractures, or change in biology. In such cases, it is often necessary to implant prosthetic material in to the site of bone loss to repair the defect (Khurana 2009). The most common and oldest technique is the implant of metals for bone repair, with new casting techniques being developed to produce porous metal structures, like porous titanium alloy (Zhao et al. 2008) and stainless steel (Kannan et al. 2005). However, metals are too stiff to promote proper bone formation, with their Young's moduli being an order of magnitude greater than natural bone. This mechanical mismatch leads to insufficient stress on bone resulting in bone resorption, excessive bone loss, and implant loosening (Ryan et al. 2006). Another problem is that metal implants must be chemically treated or coated with bioactive substances to allow bone and tissue growth on the surface (Nishiguchi et al. 2003). The additional material/material interface creates an additional possible failure point.

In addition to metals, calcium phosphate, PMMA cements, and bioactive glass have been used to fill bone defects with limited success due to lack of proper mechanical strength and pore structure (Deville et al. 2006; Jones et al. 2007; Pietrzak 2008). However, their benefits have lead to the development of ceramics and polymers for bone regeneration.

Ceramics have been used for bone repair due to their biocompatibility and good compress strength. Calcium phosphate, calcium hydroxyapatite, and tricalcium phosphate are widely used,

and, when combined with growth factors, these ceramics act as scaffolds where osteoprogenitor cells proliferate and differentiate into osteoblasts. These can be manufactured easily and availability is not a concern.

Unfortunately, a significant hurdle in wide-scale use of ceramics is the poor elastic modulus resulting in brittle materials that are prone to fractures (Deville et al. 2006). Even with the significant shortcomings for all these materials that have been discussed, the most damning issue is that they do not perform the non structural functions of bone. Natural bone is a reserve of minerals. It produces blood cells and has regulatory functions. Because of this lack of vascularization, surrounding tissue necrotizes, resulting in implant loosening in non-organic implants. Eventually infection and toxicity dominates, resulting in an average implant lifespan of 15 years. Young people have to undergo multiple revision surgeries in their lifetimes, while elderly patients cannot take the stress of repeated surgeries (Sargeant and Goswami 2006).

Using a material similar to native bone can eliminate the problems associated with using non-organic implants. Allografts, tissue from another individual of the same species, are a good option as they are available in a variety of shapes. The grafts are treated to remove immunogens to prevent adverse immunological responses in the patient. The problem is that this kind of processing removes the bone morphogenic proteins that facilitate the infiltration of mesenchymal cells into the graft and induce differentiation into bone cells, reducing the effectiveness of the treatment (Habibovic and de Groot 2007). In spite of donor screening and treating the graft, considerable risk of transmitting bacterial, viral and fungal infection to the patient exists. Finally, the graft could be rejected by the patient's body.

Autografts are considered as the best choice for implants. They are a patient's own tissue harvested from a healthy site. This removes the possibility of disease transmission and adverse

immunogenic response. There are significant challenges to autografts. This technique is possible only in cases when small quantities of tissue are required; tissue may not be available in the required shape; and the process of harvesting autogenous bone involves donor site morbidity, significant pain, blood loss, donor bone fracture and infection in a previously healthy site (Pietrzak 2008). Complications can occur if the host bone does not replace the graft (auto or allograft). One such complication is late graft fractures, as have been reported in 60% of cases from 1996 to 2006 (Cancedda et al. 2007). In many cases, tissue engineered material is the better option.

Tissue engineered material uses cells from the patient's body and has the same advantages as using autografts without some of its disadvantages. Future therapies for bone repair will be based on generation of native bone combined with degradation of an underlying scaffold. Transplantation of highly porous scaffolds seeded with bone precursor cells holds great promise in providing complete regeneration of bone and restoration of its function (Sikavitsas et al. 2001). Studies show that polymer scaffolds seeded with cells give rise to organized tissue through guided growth(Vacanti 1988). Polymeric material such as PLGA, PLA, and PGA have been shown to degrade and get absorbed harmlessly *in vivo* (Marler et al. 1998).

The most common biodegradable polymers being used or studied as potential implants include polylactic acid (PLA), polyglycolic acid (PGA), copolymers of PLA and PGA (PLGA), polyanhydrides, polycarbonates and polyfumarates. PLA and PGA, the most widely used biodegradable polymers, are aliphatic polyesters. Other useful polymers include poly(anhydride-co-imide) for weight bearing applications, poly(BPAcarbonate), which has high mechanical strength, and Tyrosine-derived polycarbonates that exhibit excellent biocompatibility for tissue regeneration (Agrawal and Ray 2001).

The polymer scaffold is often coated with osteoinductive bioactive factors to improve the rate of new bone formation (Shin et al. 2003). Further, the rate of polymer degradation can be controlled by varying functional groups, polymer architecture, and polymer blend compositions. This allows bone cells to proliferate at the optimum rate. A highly porous scaffold with interconnected pores permits migration of cells and diffusion of oxygen and nutrients into the interior. Pore sizes of 100-400 μm are optimal for good bone ingrowth (Otsuki et al. 2006).

Interconnectivity of pores is also important. Scanning electron microscopy (SEM) and mercury intrusion porosimetry are currently used for material characterization. However, both these techniques require destruction of the sample and do not assess the precise interconnectivity of pores. X-ray microcomputed tomography (micro-CT) can remove these limitations. We can obtain the internal structure of the scaffold precisely. An image-based model will automatically incorporate aspects of the actual structure that are likely to be missing from an idealized representation of the scaffold. Building a pore-scale model based on the actual image will allow us to understand fundamental microscale behavior and to investigate combinations of parameters that could not be studied experimentally without unreasonable time or cost.

2.2 Literature Review

This section is divided into two parts, experimental studies and computational work that have been done on cell seeding and proliferation in a 3D biomaterial scaffold in the past.

2.2.1 Computational Studies

Computational work in tissue engineering to date has been in developing models for cell proliferation and growth or tissue differentiation and regeneration in scaffolds seeded with cells, or map fluid velocity and shear inside a porous scaffold.

Shanbhag et al. (Shanbhag et al. 2005) developed a model for bone cell growth that predicts how cell concentrations evolve in time within a scaffold with regular pore geometry. The model assumes a uniform cell and nutrient concentration in the scaffold at the start of the simulation. The media in the bath in which the scaffold is submerged is assumed to be continuously replenished, so that the bulk concentrations of the nutrient and product (metabolic waste) are maintained at 1 and 0 respectively. The mass balance on the nutrient gives a first order partial differential equation in the normalized cell concentration that is integrated subject to initial and boundary conditions. The mass balance on the cell gives a first order partial differential equation in the normalized cell concentration and is integrated subject to initial conditions. Time interval between nutrient consumption and ejection of metabolic waste into the medium is assumed to be negligibly small. Cell growth rate is calculated using a modified Contois growth Equation.

Initial conditions:

- normalized nutrient concentration=1
- the normalized product (metabolic waste) concentration = 0
- normalized cell concentration=1

Boundary conditions:

- normalized nutrient concentration at the surface=1
- normalized product concentration at the surface = 0

A steady state solution for nutrient concentration with depth is obtained for different velocities. Nutrient is transported deeper and therefore cells are found deeper within the scaffold as velocity increases.

VanGordon et al studied the effect of porous scaffold architecture in the growth and differentiation of mesenchymal stem cells cultured under flow perfusion. Flow simulations were used to pick geometrically equivalent nonwoven fibermesh and porous foam scaffolds with similar wall shear stress distribution for comparison. Experimental results show higher initial cell proliferation and faster cell differentiation in the nonwoven fibermesh scaffolds compared to the porous foam scaffolds. The explanation for the observed difference is that cells seeded on to nonwoven fibermesh scaffolds were able to grow on to neighboring fibers, while cells seeded upon porous foam scaffolds probably needed to first lay down extracurricular matrix (ECM) and then migrate to make cellular connections before cellular proliferation and differentiation could occur (VanGordon et al. 2010).

2.2.2 Experimental Studies

Experimental work is grouped by the factor affecting cell seeding and proliferation in a 3D scaffold.

- **Surface Flow**

The nature of flow through the scaffold has an impact on the cell seeding efficiency and the pattern of cell attachment within the scaffolds. Seeding efficiency is important since there is a limit to the number of cells that can be harvested from a donor. However, there are several complicating factors. Evidence indicates that there is an optimum cell seeding density for a scaffold to maximize cell multiplication and proliferation. Additionally flow patterns also affect differentiation/mineralization of bone cells in the scaffold. Based on these criteria, we will discuss different seeding methods.

Seeding a scaffold under static conditions means that the scaffold is submerged in a medium-based cell suspension. The advantage of this method is its ease of implementation. Experimental

studies have been performed to quantify the fraction of cells that attach to the scaffold under static seeding conditions. In a study on PLGA 75/25 scaffolds seeded in static conditions (Holy et al. 2000), the percentage of cells anchoring to the scaffold after 1 h was found to be a maximum of 25% of initial cell loading, which is a low seeding efficiency. Scaffolds were placed in a culture dish each containing medium with cells suspended in it at concentrations ranging from 0.5 to 10×10^6 cells/cm^3. After 1 hour, the scaffolds are removed and the cells remaining on each culture dish were counted and expressed as a percentage of the total number of cells present at the start in the medium. This value is deducted from 100 and is taken as the cell seeding efficiency. A maximum of 25 % cell seeding efficiency is seen. A plateau of 1.5×10^6 cells/cm^3 of the scaffold volume was reached for cells remaining on the scaffold, regardless of the concentration of cells in the medium at the start of the process. Only the maximum value is reported, whereas the range of cell seeding efficiency values obtained is not reported in the paper. A major disadvantage associated with static culturing conditions is that they result in inhomogeneous cell distribution, confining the majority of the cells to the outer surfaces of the scaffold (Botchwey et al. 2001; Freed and Vunjak-Novakovic 2000; Sikavitsas et al. 2002).

Dynamic seeding technique is a seeding method where a scaffold is placed in a medium with cells suspended in it and the medium (and cells) is made to flow by inducing a centrifugal or laminar flow. Seeding techniques employing laminar flow are called perfusion cultures. Comparing dynamic versus static seeding technique we find that there is no difference in the number of cells attached, however, dynamic technique results in a more uniform distribution of cells (Gomes et al. 2003; Weinand et al. 2009).

Comparisons made between the centrifugal and laminar flow (perfusion) methods have indicated significant differences. Nutrient supply is inferior when centrifugal force is used for cell seeding compared to laminar flow conditions (Weinand, Xu et al.2009). The pattern of cell attachment and differentiation observed are also found to be different. In scaffolds seeded with mesenchymal stem cells, bone rods are found only in the peripheral region when cultured in a spinner flask, whereas bone rods are found throughout the scaffold when cultured in perfused cartridges. Additionally, hydrodynamic shear patterns are different in these two cases. In a spinner flask the scaffold periphery experiences turbulent shear and the scaffold interior experiences no shear. In a perfused cartridge there is laminar shear throughout the scaffold volume. These results suggest that stem cell differentiation is shear dependent (Meinel, Karageorgiou et al. 2004).

Perfusion aids seeding efficiency as long as both the flow rate and the cell seeding density are within a range that avoids cell detachment; there is low interactivity between cells and scaffolds (Vunjak-Novakovic et al., 1998; Li et al., 2001; Saini and Wick, 2003; Zhao and Ma, 2005). Seeding with a perfusion rate of 0.1 mm/s resulted in only 42% of the initially seeded cells to attach to the scaffold and a non-uniform cell distribution. Perfusion at 1mm/s and 10 mm/s resulted in 81% and 84% seeding efficiencies and uniform cell distribution within the scaffold (Wendt et al. 2003).

Perfusion cultures can be unidirectional or oscillatory (alternating flow direction).The advantages of oscillatory perfusion over unidirectional perfusion culture are uniform cell proliferation and differentiation. Since only a small volume of medium is required in an oscillatory perfusion culture, it is more economical when using expensive growth factors. It is an efficient technique for seeding low-cell numbers onto scaffolds (Du et al. 2008).

Although oscillatory perfusion cultures have many advantages there are some problems associated with this technique. Seeding efficiency, as defined by the percentage of cells retained in the scaffold at the end of the seeding process, is better by oscillatory perfusion compared to unidirectional perfusion and static culture. However, the seeding process in oscillatory perfusion is significantly slower, take several hours to days (compared to 1-2 hours for unidirectional and static seeding) (Alvarez-Barreto et al. 2007). Additionally, it also requires large fluid pumps to overcome the capillary resistance offered by small pore sizes of about 100 μm of the scaffold. An alternative to this method is using surface acoustic waves (SAWs) to drive cell suspensions into the scaffold. Seeding can be completed in less than 10s and seeding efficiencies, defined as the number of cells within the scaffold to that in the original suspension, of 85% can be achieved (Bok et al. 2009).

2.2.2.1 Pore Structure

Cell proliferation and attachment pattern have been shown to be a function of the pore size, shape and interconnectivity. Increased cell proliferation has been observed in scaffolds with better interconnectivity of (Gomes et al. 2003). In scaffolds with pore sizes greater than the cell size, cell attachment increases linearly with the specific surface area of the scaffold (O'Brien et al. 2005). Cell penetration is found to be better in scaffolds with irregular pores compared to scaffolds with uniform and straight pores. This may occur because irregularity in pore size causes recirculation of fluid inside the primary pores and convects the fluid (and cells) to the secondary pores. Compared to uniform and straight pores, in irregular pores higher shear stresses generated due to recirculation and higher bulk convective velocities causes particles to detach from pore walls and move deeper into the scaffold (Bok et al. 2009).

The bulk of previous research done on cell seeding is experimental, with qualitative results. Even computational studies on colloid transport in a porous media do not take into account the disordered structure of a real porous media and predict the particle deposition pattern. There is no computational model available, which incorporates the internal structure of a real porous material, and which can therefore shed light on the effect of the internal structure of the porous material and the flow conditions on particle transport and the resulting deposition pattern in a disordered porous material. Such a model could be used for studies on cell seeding in a real polymeric scaffold to understand the extent to which the scaffold internal architecture and flow conditions could affect the cell attachment pattern. Our research aims to fill this gap, by developing an image-based computational model for particle transport and attachment in a porous material that incorporates the real internal structure of a disordered porous material.

CHAPTER 3 SIMULATION OF PARTICLE MOVEMENT AND ATTACHMENT IN A POROUS MATERIAL

A high quality 3-D grayscale image of the porous material where the solid and the pore space are clearly separated is the starting point for image-based modeling. Using this image, the pore space is discretized into tetrahedral elements to facilitate numerically solving the fluid flow equations to obtain the velocity profile. This is done using an in-house mesh generation code.

Following mesh generation, numerical modeling of flow is performed by numerically solving the relevant Equations of Motion (numerical discretization) to obtain the velocity profile inside the void space. Forces on the pore surfaces are also computed in this step. In our research, we develop a model that can be used to study the relationship between forces acting on the colloidal particle and the attachment pattern of particles in the porous media. These forces are in turn dependent on pressure drop across the porous material, the porous material's internal architecture and properties of the colloidal particle and the fluid (medium) in which the particles are suspended. Numerical simulations of flow and particle attachment are performed in a three-dimensional disordered porous material, and the attachment of particle to the porous material surface is simulated.

The following assumptions are made in our model for particle movement and attachment in a disordered porous material. We assume low Reynolds number flow (-implying that inertial forces are small compared with viscous forces), that the particle concentration in the media is dilute (to treat the particle movement and attachment process as being equivalent to sending particles sequentially into the porous material) and that the model is suitable for colloid particles. Each particle is tracked until it either flows out of the porous material or attaches to a pore

surface. Figure 2 shows the flow chart for simulating particle motion and attachment of a single particle in a heterogeneous scaffold.

3.1 Velocity Calculations

The finite element method (FEM) is a numerical method used to obtain approximate solutions to partial differential equations. This method is used to obtain velocity profiles by an in-house FEM code developed specifically for modeling Stokes flow in porous materials. This FEM based code was not developed as part of this research and the description provided in this work provides only the basic information from an end user's perspective.

The FEM code uses a tetrahedral mesh with P2P1 Taylor-Hood elements. This element uses a quadratic approximation for velocity and a linear approximation for pressure. A mixed Bubnov-Galerkin method is applied to the Stokes Equations and the approximation functions are inserted into the resulting weak form of the equation.

Boundary conditions applied to the problem are:

- No slip at the void-solid interfaces.
- Surface tractions over inlet and outlet regions.

Solution to the linear system of Equations yields velocity and pressure at the nodal points of each element. These same parameters can be determined at any point within the domain by interpolation from the solution set. Additional details can be found in works by Huebner (Huebner et al. 1995) or Lane (Lane and Thompson 2010).

3.2 Stochastic Method

Convection, diffusion and electrostatic forces affect particle displacement. While the convective and electrostatic force calculations are deterministic, diffusion can be modeled by an appropriate random walk process. The particle tracking algorithm is run by sequentially releasing a large number of particles from the porous media inlet and following their motion as governed by convection, electrostatics, and diffusion, the latter of which is described by Equation (1). The particle is followed until it either escapes from the porous media or attaches to the pore surface. The Equation for a diffusive 3-D random walk is expressed as follows (Guo et al, 2003):

$$\Delta \boldsymbol{r} = \boldsymbol{u}\Delta t + \sqrt{6D\Delta t}\,\boldsymbol{\xi} \tag{1}$$

In this form of the equation $\Delta\mathbf{r}$ is the total displacement, Δt is the time step, **u** is the velocity, D is the diffusion coefficient and $\boldsymbol{\xi}$ is a three-dimensional vector whose elements are selected randomly from a Gaussian distribution with zero mean and unit variance.

If a constant timestep Δt is set for all the calculations based on the highest velocity in the pore space, it will take many time steps for the same displacement in a region of low or intermediate velocity, which in turn will make calculations computationally inefficient. This problem is solved by adjusting the time step according to the velocity at that point so that each particle moves a constant distance at each step. The time step Δt is calculated from Equation (2) for the three-dimensional case.

$$\delta_{\mathrm{M}}=|\mathbf{v}(\mathbf{r})|\Delta t+\sqrt{6D\Delta t} \tag{2}$$

where δ_M is the uniform characteristic displacement length, D is the diffusivity of the cell and **v(r)** is the sum of the velocity due to convection and electrostatic forces. The uniform characteristic displacement length is set to a constant value.

3.2.1 Electrostatic Force Calculations

Analytical expressions are used for forces in the Van der Waals and the electrical double layer cases, due to particle-plane interactions within the Derjaguin–Landau–Verwey–Overbeek (DLVO) framework (Zypman 2006). The expressions are valid for colloidal particle interactions in the aforementioned geometry. Although our geometries are significantly more complex, we use this approach as a first approximation because it offers an explicit form of the necessary force computation, which is essential to maintain numerical efficiency. Additionally, because the surfaces of the elements are planar (in the meshed version of the pore space), this assumed geometry is appropriate.

The expression for the force between the sphere and the plane for a case of Van der Waals interaction is given by Equation (3):

$$F(d) = -\frac{A_H}{6}\left[\frac{a}{d^2} + \frac{a}{(d+2a)^2} + \frac{1}{d+2a} - \frac{1}{d}\right] \tag{3}$$

where A_H is the effective Hamaker constant, d is the distance of closest approach between the sphere and the plane, and a is the radius of the sphere.

The expression for force due to Electric double layer interaction is obtained from Equation (4):

$$F(d) = 2\pi a\left[32\varepsilon_0\varepsilon_r\kappa \tanh\left(\frac{ze\psi_1}{4kT}\right)\tanh\left(\frac{ze\psi_2}{4kT}\right)\left(\frac{\kappa T}{ze}\right)^2\right]\left[\left(1-\frac{1}{\kappa a}\right)+\left(1+\frac{1}{\kappa a}\right)e^{-2\kappa a}\right]e^{-\kappa D} \tag{4}$$

where ε_0 is the vacuum permittivity, e is the elementary charge, ε_r the permittivity of the electrolyte, z is the valence in a symmetrical electrolyte, κ is the inverse Debye length, $\psi_1$and ψ_2

are the electrostatic potentials at each plane, k is Boltzmann constant, and T the absolute temperature.

Adding the Van der Waal's force from Equation (3) and the electrical double layer force from Equation (4) gives the magnitude of the DLVO force acting on the particle in a direction normal to the pore surface. Multiplying the magnitude of the DLVO force with the vector opposite in direction to the unit normal from the pore surface gives the DLVO force vector $\boldsymbol{F_{dlvo}}$. To determine the effect of this force on the fluid motion, we consider that the fluid through which the particle moves offers a resistance in the direction opposite to the motion of the particle. The Equation for viscous resistance is as shown in Equation (5).

$$\boldsymbol{F(D)} = -C_D\boldsymbol{v} \tag{5}$$

In this expression C_D is the drag coefficient and $\boldsymbol{v}$ is the velocity. In the low Reynold's number flow regime, which is the regime our simulation is set up for, the drag coefficient is given by Equation (6).

$$C_D = 6\pi\rho a \tag{6}$$

Where ρ is the viscosity of the medium and a is the diameter of the particle.

Substituting the DLVO force, $\boldsymbol{F_{dlv,o}}$ into the combined expression of viscous resistance from Equations (5) and (6) and rearranging results in the expression for velocity acting on the particle in the direction normal to the pore surface, we arrive at Equation (7).

$$\boldsymbol{v} = -\left[\frac{F_{dlvo}}{(6\pi\rho a)}\right] \tag{7}$$

In the algorithm, this equation is used to factor in the contribution of electrostatic forces to the total velocity acting at the center of a particle.

3.2.2 Criteria to Decide the Starting Location of a Particle

Starting points are at the inlet of the porous material on an imaginary plane perpendicular to the direction of flow of the medium. Particles are released randomly from this plane but with a flowrate bias, which reflects the fact that more particles will enter in the regions that are carrying more flow. To perform this computation, we first loop through a grid of points in the plane and make a cumulative distribution of the ratio of flow rate at a point to the total flow rate across the inlet plane. The cumulative flow rate distribution is mapped to the starting position at the inlet of the porous material. Random numbers from 0 to 1 are mapped to this cumulative flow rate distribution. A random number is generated at the beginning of the iteration, and the starting point is selected according to this flowrate-biased random selection.

3.2.3 Condition for Particle Attachment

When the particle comes very close to the pore surface, a combination of the direction of streamlines and electrostatic interactions determine particle attachment to the pore surface, as shown in Figure 1. We focus on how the porous material's internal structure and the fluid mechanics affect the attachment of the colloidal particle to the interior surface of the porous material.

F_E in Figure 1 is defined as in Equation (8).

$$F_E = -F_{dlvo} \tag{8}$$

where $\boldsymbol{F_{dlvo}}$ is the DLVO force vector. F_E is defined in such a way so that a positive sign would correspond to a direction into the pore surface. F_S in Figure 1 is the force on the particle due to convection given by Equation (9).

$$\boldsymbol{F_S} = \frac{\boldsymbol{v} \times mass}{\Delta t} \tag{9}$$

Where $\boldsymbol{v}$ is the convective velocity, *mass* is the mass of a particle and Δt is the timestep. Note that F_E and F_S are acting at the center of the particle. The particle attaches to the surface when the condition in Equation (10) is satisfied.

$$F_E + F_{S\ perpendicular} \geq 0$$

Where F_E is the electrostatic force and $F_{S\ perpendicular}$ is the component of convective force normal to the pore surface.

Particles that do not attach to the pore surface flow out of the porous material. The velocity profile in the porous material is not recalculated to account for change in the internal geometry caused by particle attachment, as we are analyzing each particle as a unique, independent event. The model predicts the probable attachment locations of particles introduced into the porous material.

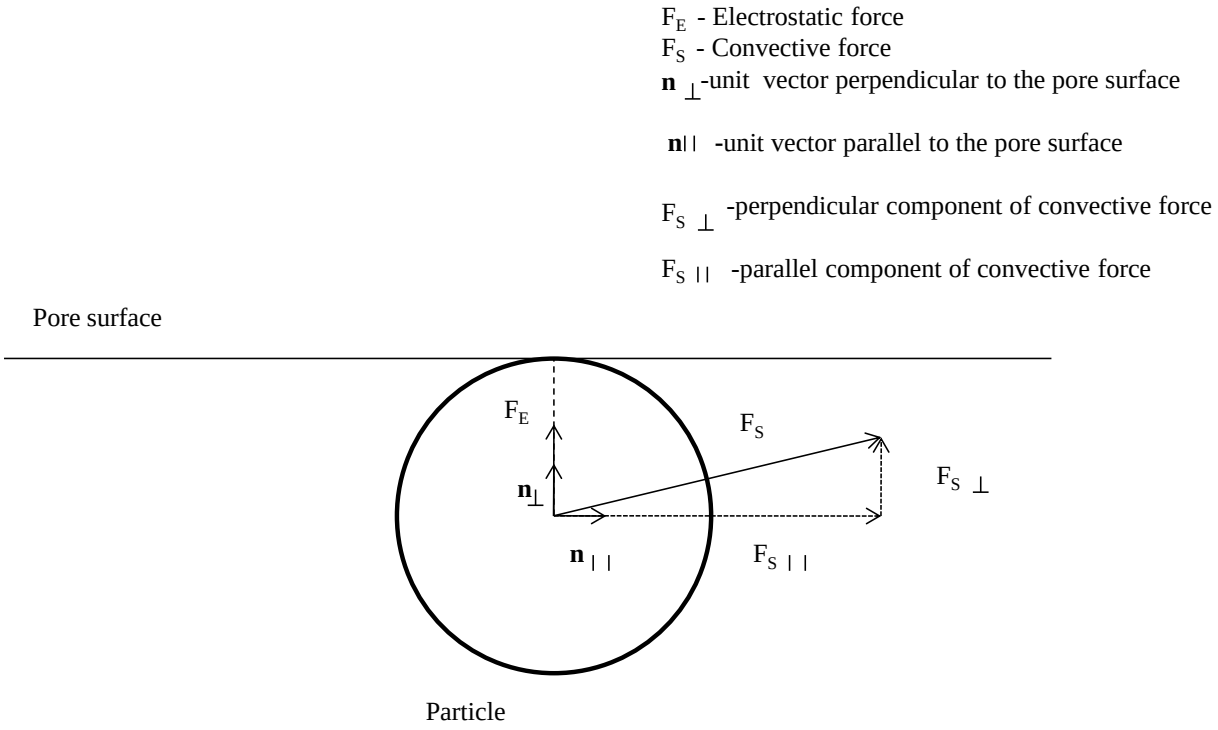

Figure 1: Particle attachment schematic

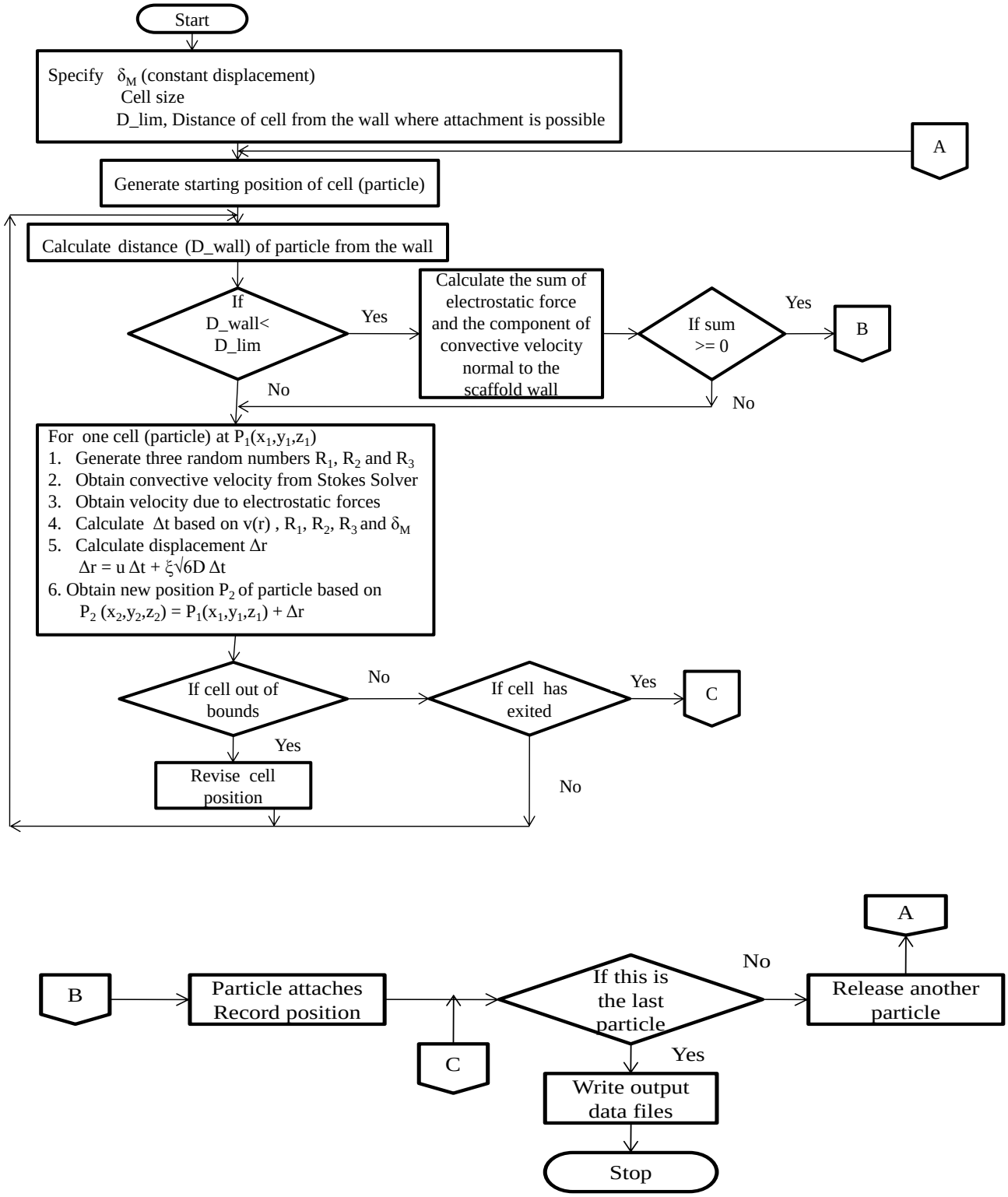

Figure 2: Flowchart for particle tracking algorithm

3.2.4 Application of the Model to a Simple Geometry

It is difficult to test a model for being physically realistic by applying the model to a complex geometry. The model for particle movement and attachment in a porous media can be applied to a few simple geometries for the purpose of debugging and to get a sense of the factors controlling particle attachment. It is important to pick a geometry that resembles a portion of a typical porous material. The suitable simple geometry should have:

(i) Stagnation point

(ii) Narrowing and widening of the channel.

(iii) Splitting and rejoining of streamlines.

(iv) Confined, Poiseuille-type flow

A number of options could be chosen for simulations on a simple geometry; we chose a cylinder with a sphere fixed inside it, which fluid must flow around. This geometry satisfied all the previously mentioned requirements (see Figure 3).

Inlet conditions:

- Dimensionless pressure at the inlet is set to unity and pressure at the outlet is zero.

Conditions under which the simulation was performed:

- Dimensionless particle diameter: 4.0
- Number of particles injected: 10,000
- Concentration of the electrolyte (NaCl used in test case) in the medium: 0.1M
- Dimensionless characteristic length δ_M : 0.2
- Peclet number: 1×10^{-4}

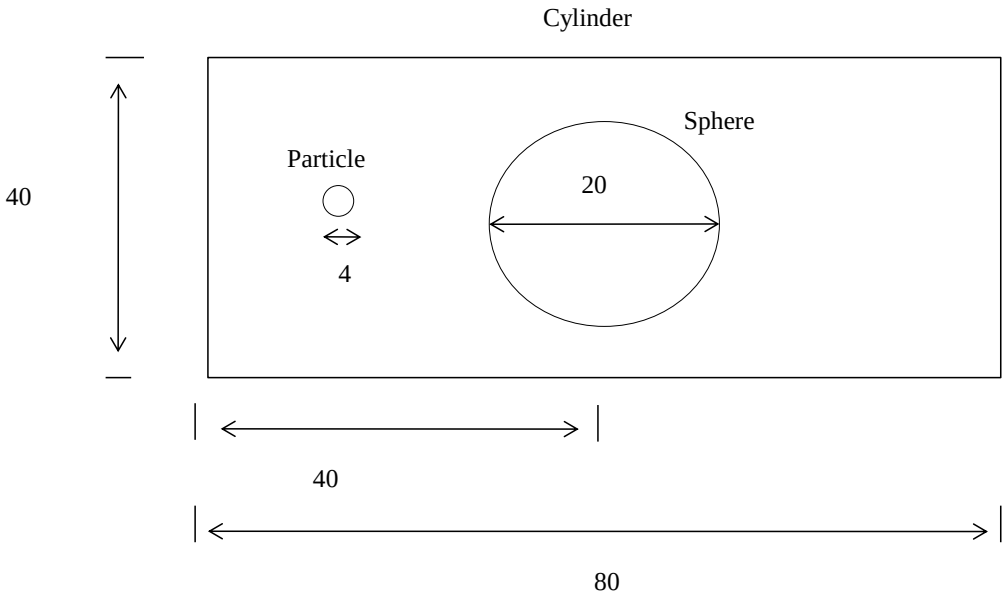

Figure 3: Proportions of the simple geometry.

From the pattern of cell attachment in Figure 4 it is apparent that attachment occurs almost exclusively upstream of the plane normal to the cylinder wall that passes through the sphere center point. This makes sense for a system in which diffusion is small relative to convection (i.e., a high Peclet number), because once a particle passes the embedded sphere, all convective motion takes the sphere away from the wall.

Figure 12 is a 2D view of streamlines on the upper half of the horizontal centerline in the simple geometry. Figure 12 may help to explain the attachment pattern in Figure 11. The direction of the streamlines downstream is away from the wall causing the cells to be pulled away from the wall which explains why there is no attachment downstream. The low velocity zone around the obstruction (sphere) and at the cylinder walls is a diffusion dominated zone where most of the cells attach.

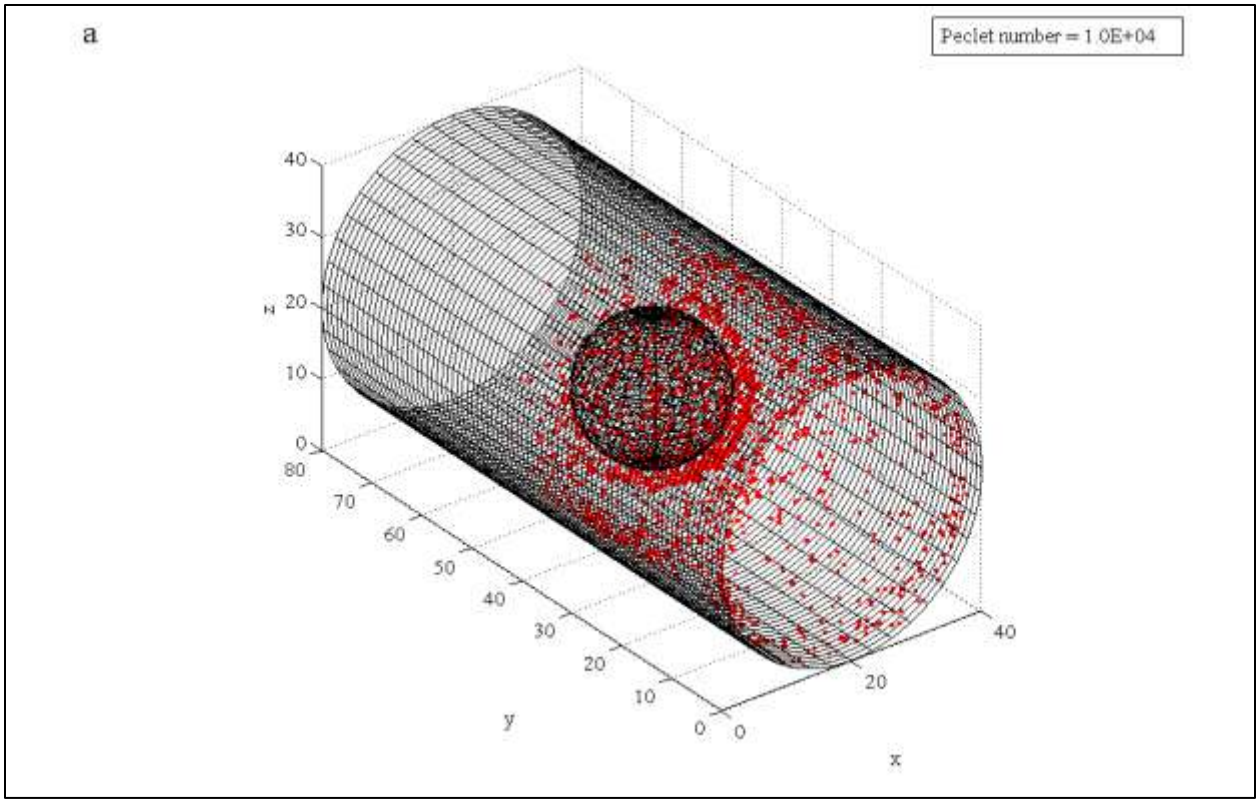

(a)

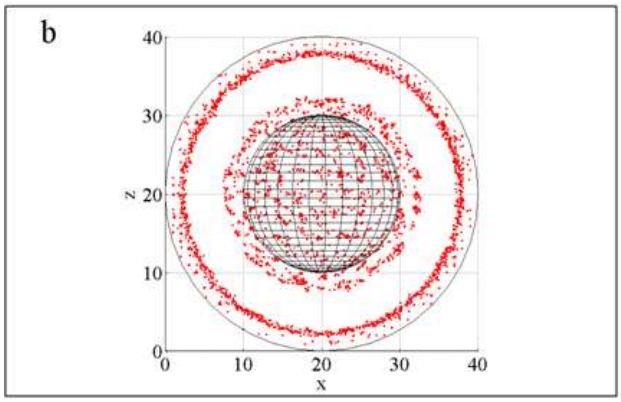

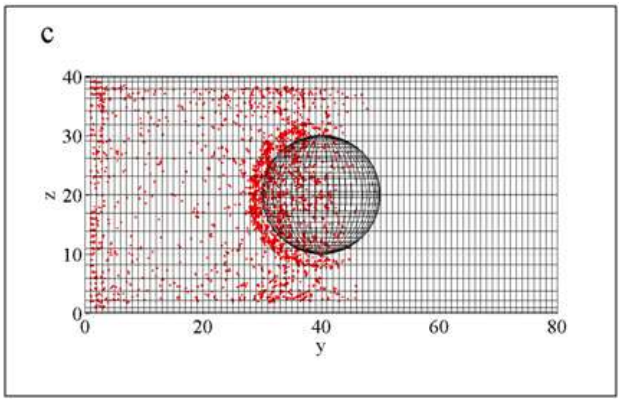

(b) (c)

Figure 4: Attachment pattern in a simple geometry; the red dots denote the center of the particle (a) 3 D view (b) XZ plane (c) YZ plane

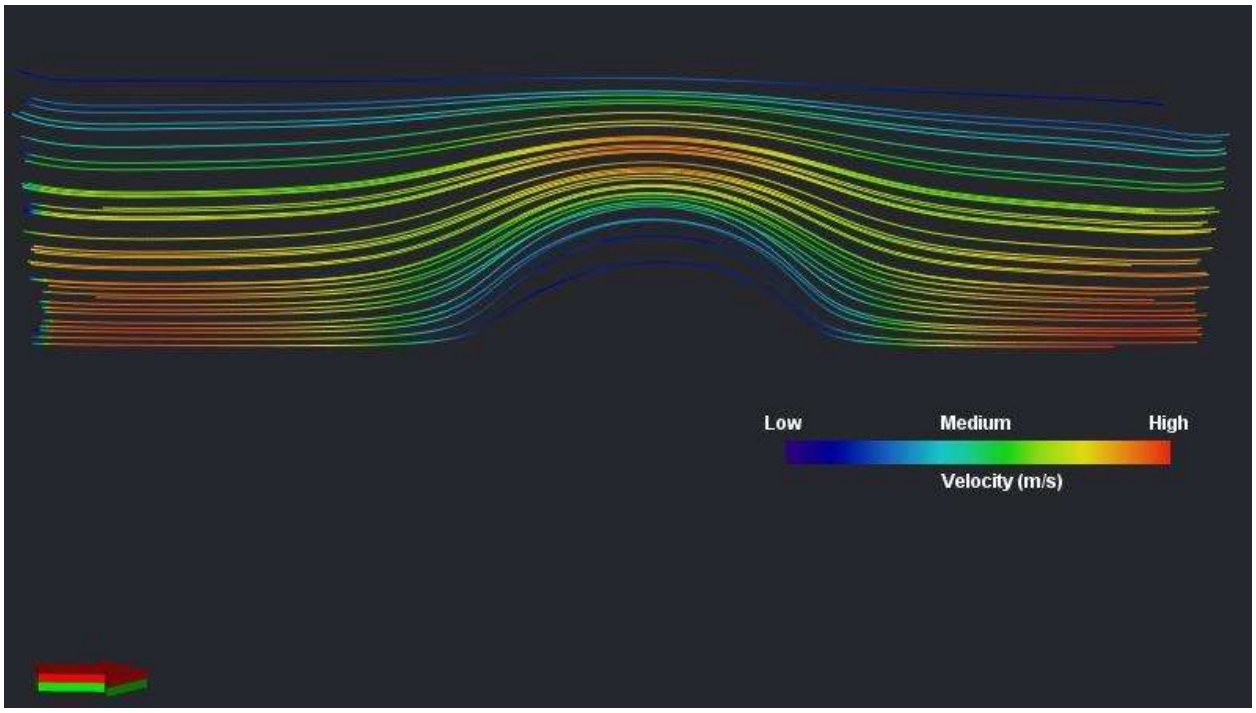

Figure 5: Velocity profile in a simple geometry; 2D axisymmetric view.

CHAPTER 4 APPLICATION OF THE MODEL TO TISSUE ENGINEERING/CELL SEEDING

Our model for particle movement and attachment in a disordered porous material which has been tested in a simple geometry is now suitable to be applied to different problems. Our test problem will be prediction of the movement and attachment of bone cells in a porous scaffold during the process of cell seeding, as this was the motivation for the work. We demonstrate this concept in following chapter. For this work, the heterogeneous porous material used in our simulation is based on the image of a real disordered biological polymeric scaffold that we made using the salt leaching method (see below).

4.1 Experimental Procedure: Sample Preparation

To fabricate porous polymeric scaffolds, a salt leaching technique (Datta 2007) is used. Sodium chloride crystals are sieved and only those remaining between 75 μm and 250 μm mesh sizes are retained. The sieved salt crystals are placed into an acrylic tube (D=3 mm, L=6 mm), which is covered with citroseal capillary sealant at one end. Poly ethylene glycol (PEG)-400(10g), diphenyl (2,4,6 trimethyl benzoyl)- phosphine oxide/ 2-hydroxy-2-methyl propionate 50/50 (1ml) (photoinitiator or PI) are vortexed (VORTEX-GENIE 2, .65 AMPS, 60 Hz, 120 V) to form a solution. The mixture of PEG and photoinitiator is poured over the salt in the tube. The polymer-PI mixture penetrates into the spaces between the salt crystals. The salt/PEG mixture is centrifuged at 10,000 rpm for 10 minutes. This step improves penetration of the PEG-PI mixture into the salt and produces a close packed system to maximize porosity. The tube containing the mixture is exposed to UV radiation (INTELLI-RAY 600,600 Watt UVA, 115/230 V) for a period of 40 seconds. The polymer hardens due to cross linking and the salt can then be leached out by dissolving it into injected water. This process gives a hardened polymer with pores

located where the salt crystals once were. In the sample created for 3D imaging, we obtained a sample with a porosity of 56.7% as measured by voxel count.

Imaging the scaffold after salt has been dissolved is difficult because of the low contrast between air and the crosslinked PEG. This problem has occurred when imaging PEG/air systems for other applications, and the reason is evident from attenuation data obtained from the National Institute of Standards and Technology (NIST) website (see Figure 6).

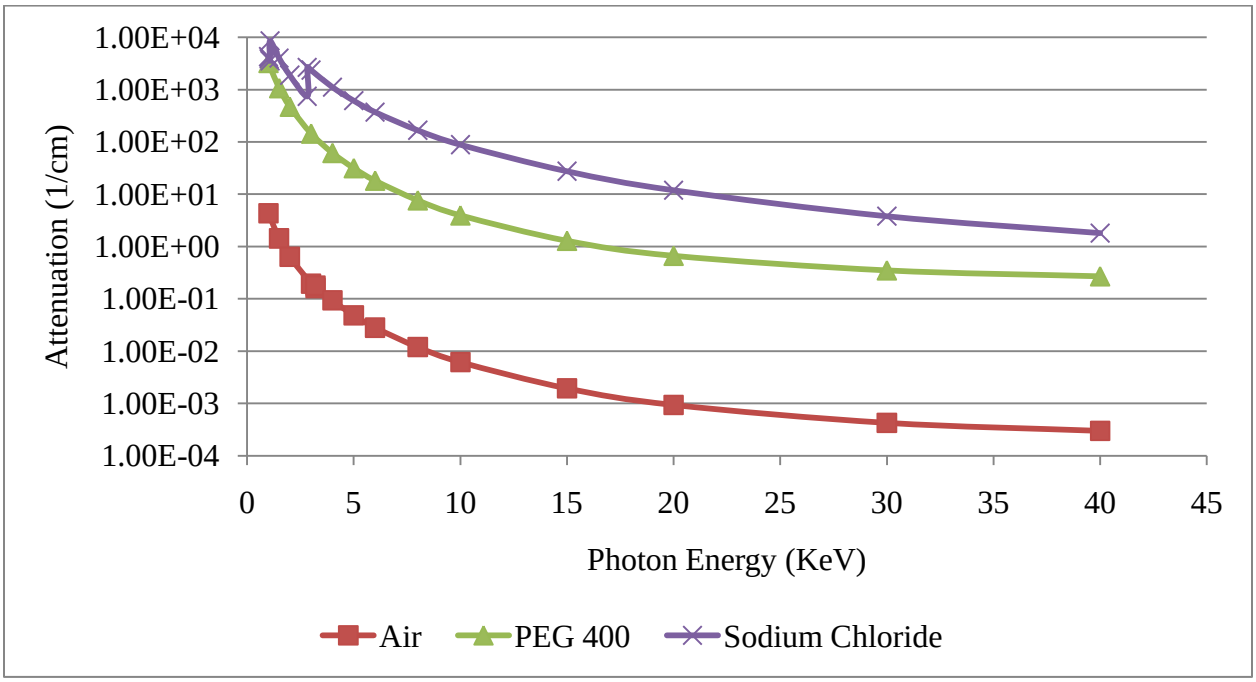

Figure 6: A comparison of Attenuation vs. Energy for different compounds (NIST)

At the x-ray energy of 40 KeV at which the imaging was performed, the attenuation for PEG 400 is 2.69×10^{-1} cm^{-1} wheras the attenuation for air is 2.98×10^{-4} cm^{-1} which is a 3 order difference in magnitude. Sodium chloride has an attenuation of 1.8 cm^{-1} that makes the order of magnitude of difference for attenuation between Sodium chloride and air to be 1. The sensitivity of the instrument is bad at the lower attenuation values due to a sensitivity limit existing for the instrument below attenuation values of 10^{-1} cm^{-1}. Therefore the XMCT image will give poor

contrast for PEG and air, whereas the image will have better contrast for PEG and sodium chloride. Hence, to obtain a good image, we imaged the scaffold before salt was leached out of the system. The contrast between the salt and the polymer provided a good image of where the pore space will be after leaching (i.e., where the salt is in the original image).

4.2 X-ray Micro Tomography Imaging and Image Processing

X-ray Computed micro Tomography (XCT) is a noninvasive technique that provides a three dimensional image of an object by mapping the X-ray attenuation through the sample onto a detector grid. XMCT imaging was performed at The Center for Advanced Microstructures and Devices (CAMD), Louisiana State University. The schematic of a typical XCT imaging set up is shown in Figure 7.

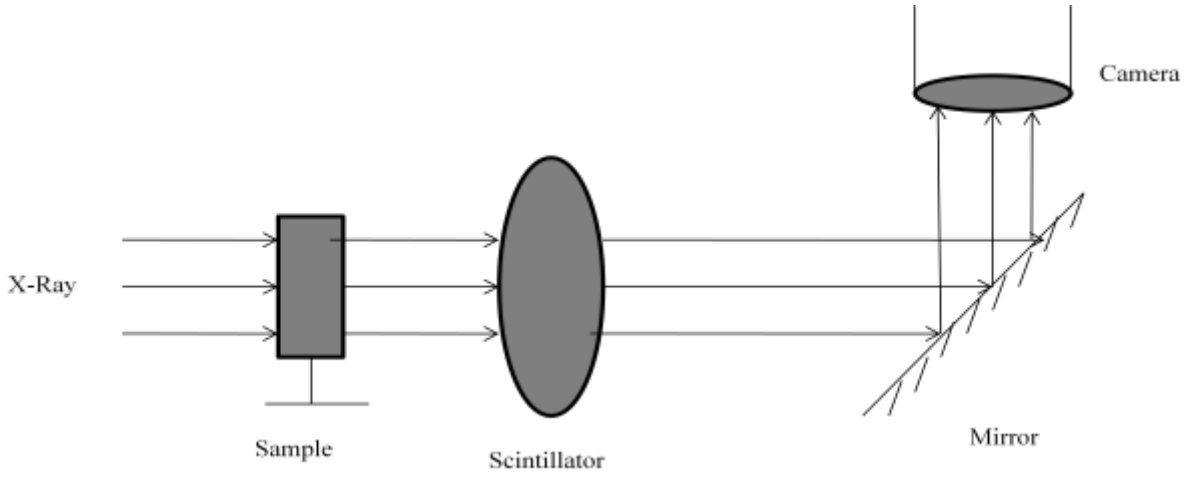

Figure 7: X-ray Micro-tomography setup

X-ray light at an energy of 40 keV is obtained from a synchrotron source. The collimated beam of X-ray light is passed through the sample. A part of the incident X-Rays is absorbed by the sample material and the rest passes through.

The Beer-Lambert Law gives the ratio of the measured to the incident X-Ray intensity, given by Equation 1 and 2:

$$\frac{I}{I_0} = e^{-\mu x} \tag{10}$$

$$\mu = \frac{\mu_M}{\rho} \tag{11}$$

where, I_0 is the intensity of the incident X-Ray beam, I is the intensity of the transmitted X-ray beam, μ is the linear attenuation coefficient of the specimen, μ_M is the mass attenuation coefficient of the specimen, ρ is the specimen density and x is the specimen thickness.

The X-ray energy that passes through the sample is converted by the scintillator to visible light so that it can be imaged using a digital camera. The camera has a lens which gives a spatial resolution of 5 µm/ pixel. A 2D projection of the 3D structure is collected via the detector. The sample mounted on the sample stage and rotated 180 degrees in increments of 0.25 degrees and a series of projections is collected. These projections along with the calibrating images (white and dark field collected without the sample) are then used to generate the 3D voxel image of the sample. For this work, a filterback projection reconstruction algorithm implemented in MATLAB is used to transform the projection images into the 3D data.

The reconstructed voxel image is grayscale in nature, meaning the voxels exhibit a range of X-ray absorbance values. To perform image-based modeling, one typically converts the grayscale image into a segmented image (meaning voxels are labeled according to the phases in the image rather than the absorbance values). For the current sample, the segmented data set will contain only two labels, corresponding to the polymer and void phases. However to achieve an

accurate segmentation of an image, noise must often be removed. One effective method for noise removal from a grayscale image is anisotropic diffusion (Bhattad et al. 2010; Weickert and Scharr 2002). The anisotropic diffusion algorithm works on the principle of removing noise from the homogeneous region of an image without altering the phase boundaries. The diffusion Equation is applied to the image and diffusion coefficient is constructed as a decreasing function of the image grayscale gradient (low gradient suggests homogeneity and high gradient suggests the phase boundaries, where the grayscale value changes significantly). Along with the grayscale gradient, the local structural details are included in the diffusion tensor so that diffusion in the normal direction to the edges (phase boundaries) is minimized, while the noise removal is done tangential to the edges, in addition to inside homogeneous regions.

After noise removal, the clean image can be segmented into its components (solid, void, etc.). We employ the Indicator Kriging algorithm for segmentation (Bhattad et al. 2010; Oh and Lindquist 1999). In this algorithm, a fraction of image voxels are assigned to two populations in the thresholding step using a two point threshold. The kriging weights are calculated from the measured (assigned) part of the partially segmented image using a two point covariance function. The probability of the value at an unassigned location being larger than the threshold is calculated as linear-weighted combinations of the kriging weights and measured values in the neighborhood.

4.3 Mesh Generation

Discretization of the void space is the second step in an image-based modeling technique. The void space of a porous medium can be represented with a mesh, either structured or unstructured (cubes or tetrahedrons), depending on the modeling strategy. In our case, an in-house mesh generation algorithm is used, which operates directly on the segmented voxel image

and generates a mesh of the pore space. The resulting tetrahedral mesh respects the original image by placing boundary nodes on the void-solid interface. A slice from the digital image and a thin section of the corresponding mesh are shown in Figure 8. (The black region in Figure 8 (a) denotes the pore space in the tomography slice). Figure 8 (b) shows a 2 D projection of the meshed volume of the scaffold in the vicinity of the slice shown in Figure 8 (a). The tetrahedrons colored blue are on the void-solid interface and have velocities known from the no slip boundary condition. The white tetrahedrons are in the interior of the void space and have unknown velocities which are solved using the FEM method. The necessary input for running the simulation is available following the meshing step and use of FEM to obtain the velocity profile in the void space.

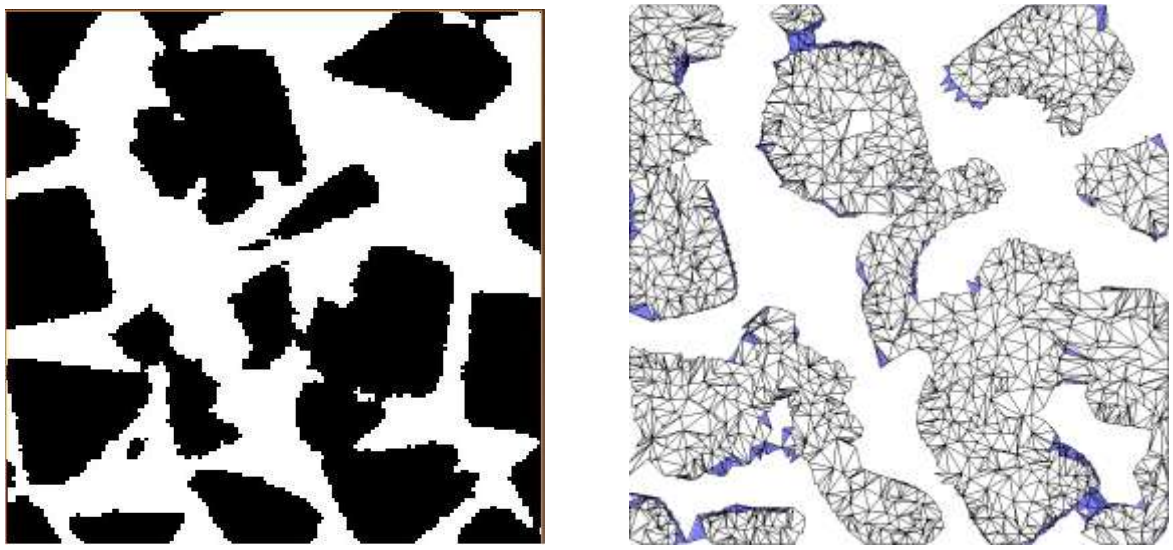

(a) (b)

Figure 8: Thin section of scaffold image: (a) segmented XMCT image showing void (black) and solid (white) (b) corresponding mesh showing regions where velocity is known (blue) and regions of unknown velocity (white tetrahedrons). It is a cropped section of volume mesh in the vicinity of the slice shown in (a); a 2 D projection of a 3 D picture.

4.4 Simulation Conditions

The simulation based on the algorithm mentioned in the previous chapter, is carried out on a small 750 µm × 750 µm × 750 µm section of the original XMCT image (displayed in Figure 3). Although the cutout of the sample is very small compared to the image of the actual scaffold which is a cylinder 3000 µm in diameter and 6000 µm in height, the simulation is run on the cutout in the current work to better understand the modeling and general behavior prior to running much more time consuming computations on larger sections of the scaffold.

The assumption that the particle concentration in the media is dilute allows us to treat the cell seeding process as being equivalent to sending cells sequentially into the scaffold. This is a reasonable assumption in that the typical cell concentration in seeding media is in the range of 2×10^6 to 10×10^6 cells/mL (Vunjak-Novakovic et al. 1998). At a lower range of 2×10^6 cells/mL cells account for 0.84 % by volume of the seeding media. The higher range at 10×10^6 cells/mL would be 4.19 % by volume of the seeding media.

Remaining conditions:

- Bone cell diameter : 20 µm
- Number of cells injected : 10000
- Concentration of the electrolyte (NaCl) in the medium : 0.1M
- Characteristic length δ_M : 1 µm

4.5 Terminology

The following definitions are used extensively in this chapter.

1) Peclet number

The Peclet number *Pe* is defined as:

$$Pe = \frac{|\mathbf{v}|L}{D} \tag{12}$$

Where **v** is the Darcy velocity of the porous material, L is the characteristic length of the porous material which is the length of the material along the direction of flow and D is the diffusivity of the fluid in which the bone cells are suspended.

The Peclet number defines the ratio between rate of transport by convection to the rate of transport by molecular diffusion(Bear 1972).

2) Darcy velocity

Darcy velocity for a porous material is defined as:

$$|\boldsymbol{v}| = \frac{Q_{inlet}}{A_{inlet}} \tag{13}$$

Where Q_{inlet} is the flow rate at the inlet and A_{inlet} is the cross-sectional area of the inlet plane.

3) Local pseudo Peclet number

We define the local pseudo Peclet number as

$$local\ Pseudo\ Peclet\ number = \frac{|\mathbf{v}| \times \delta m}{D} \tag{14}$$

Where v is the velocity of the cell at the beginning of the timestep, δm is the uniform characteristic displacement length as defined in Equation 4 and D is the diffusivity of the cell. This number is applicable at a local level and gives the ratio between rate of transport by convection to the rate of transport by molecular diffusion in a particular region where the cell is located.

4) Global Peclet number

This term is the same as the Peclet number defined previously. It applies to a domain size equivalent to the entire cutout of the scaffold on which the simulation is performed.

4.6 Results and Discussion

4.6.1 Effect of Peclet Number

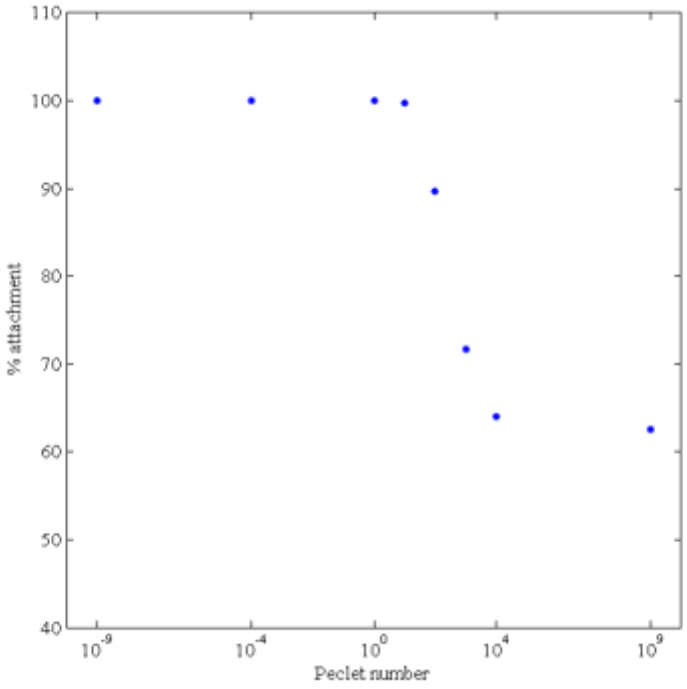

Figure 9: The effect of Peclet number on percentage cell attachment

In this section we present the effects of various factors on the attachment pattern of bone cells on a disordered biological polymeric scaffold during the process of cell seeding. We focus particular attention on the Peclet number and the type of pore geometry.

It can be seen from Figure 9 that the percentage cell attachment drops below 100 beyond a Peclet number of 10 and shows a decreasing trend until a Peclet number of 1×10^9. It can be inferred that a diffusion dominated flow regime results in a high cell attachment percentage.

Figure 10 shows the change in the pattern of cell attachment (seeding) in the scaffold with the Peclet number. For the case of Peclet number equal to 1×10^{-4} which is a diffusion dominated flow regime, it is seen that the cell attachment is limited to a 100 μm length from the inlet of the scaffold. As the Peclet number increases and the flow regime becomes convection dominated, a more even pattern of cell attachment is observed along the scaffold in the direction of flow of the medium.

To better understand behavior at the level of individual cells from the distribution in Figure 10, we compared the local pseudo Peclet number of a particle having the same starting position, at two different global Peclet numbers as it moves along a trajectory.

We can see from Figure 11 that the trajectory of a cell shows that it is in a convection dominated regime in a system with Peclet number equal to 1×10^4 and the trajectory of the same cell in a system with Peclet number equal to 1×10^2 is influenced strongly by diffusion. We can observe that for two particles starting at the same point at the two different Peclet numbers shown, the particle in the high Peclet number system ends up attaching further along the direction of flow (or not at all). More particles travel further along the scaffold in the direction of flow at high Peclet numbers, to result in a more even distribution of cell attachment as observed from Figure 10.

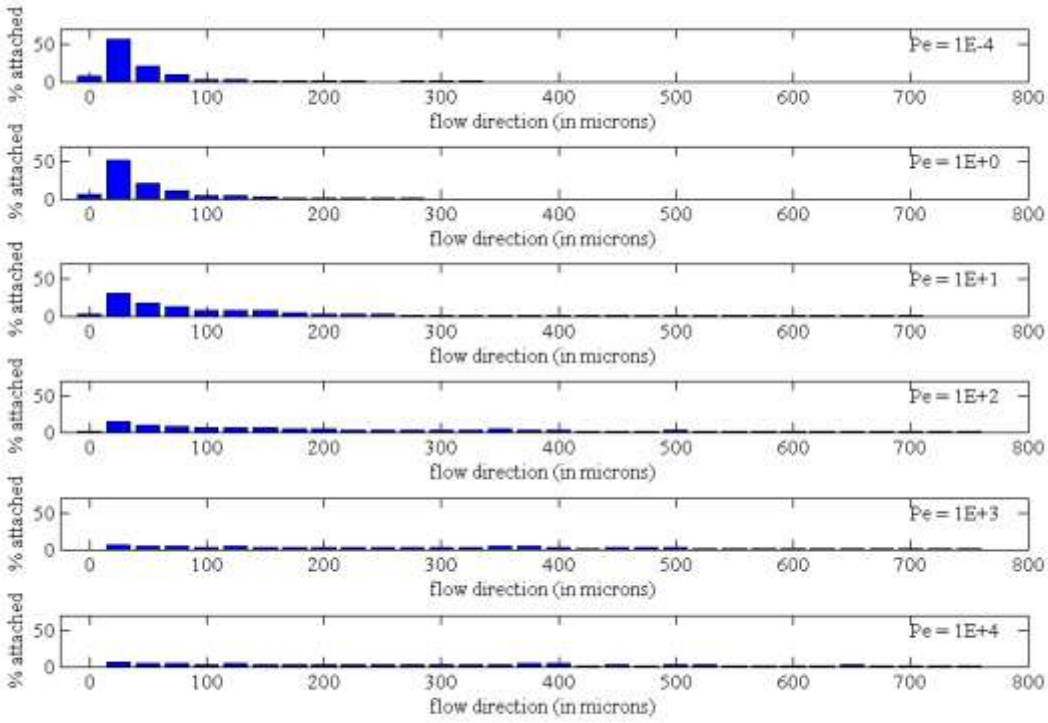

Figure 10: The effect of Peclet number on the cell attachment pattern in the scaffold

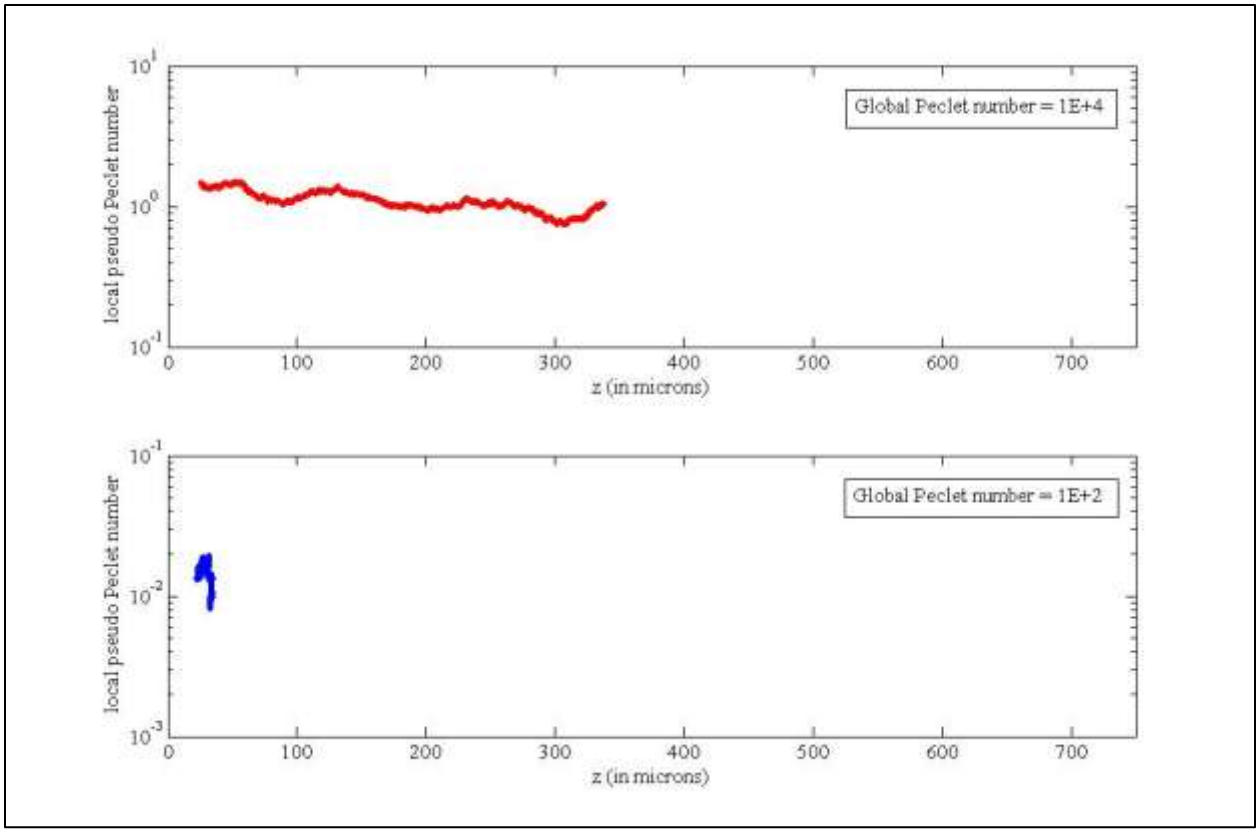

Figure 11: Comparison of particle trajectories at different Peclet numbers

4.6.2 Effect of Pore Geometry and Pore Size Distribution

Although Figure 10 shows a uniform attachment pattern at a Peclet number of 1×10^4, from Figure 12(a) the pattern of cell attachment in a scaffold appears to be spatially nonuniform, with clusters of cells attached at specific locations. Compare this image with Figure 12(b), which is a distribution of the same number of particles attached uniformly over the pore surface (independent of velocity). Figure 12 (a) is the actual attachment pattern obtained from running the simulation at a Peclet number of 1×10^{-4}. The red dots represent the center of the particle.

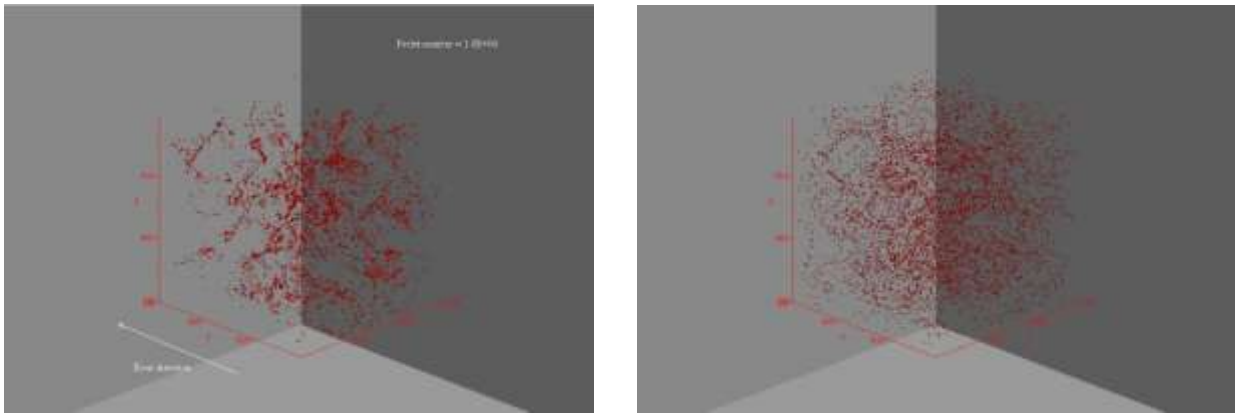

(a) (b)

Figure 12: Comparison of the attachment pattern correlated with velocity with a distribution not correlated with velocity; the red dots represent the center of the particle (a) Cell attachment pattern in a scaffold obtained from running the simulation at a Peclet number of 1 × 10-4 and therefore correlated with cell transport(b) A pattern of attachment obtained by distributing the same number of particles uniformly over the pore surface; not correlated with cell transport

From Figure 10 we know that in a diffusion dominated flow regime (low Peclet numbers) particles cluster at the inlet. From Figure 10 we see that the particle attachment becomes more uniform at high Peclet numbers but Figure 12 shows that the spatial distribution is not really uniform. To better understand why this behavior occurs, we plot the cell attachment numbers versus length for high Peclet number, along with porosity versus length. Normally, porosity would be constant as a function of length, and would not provide useful information. However, since our simulation domain is small, it may act as a simple surrogate for other parameters that might affect the process.

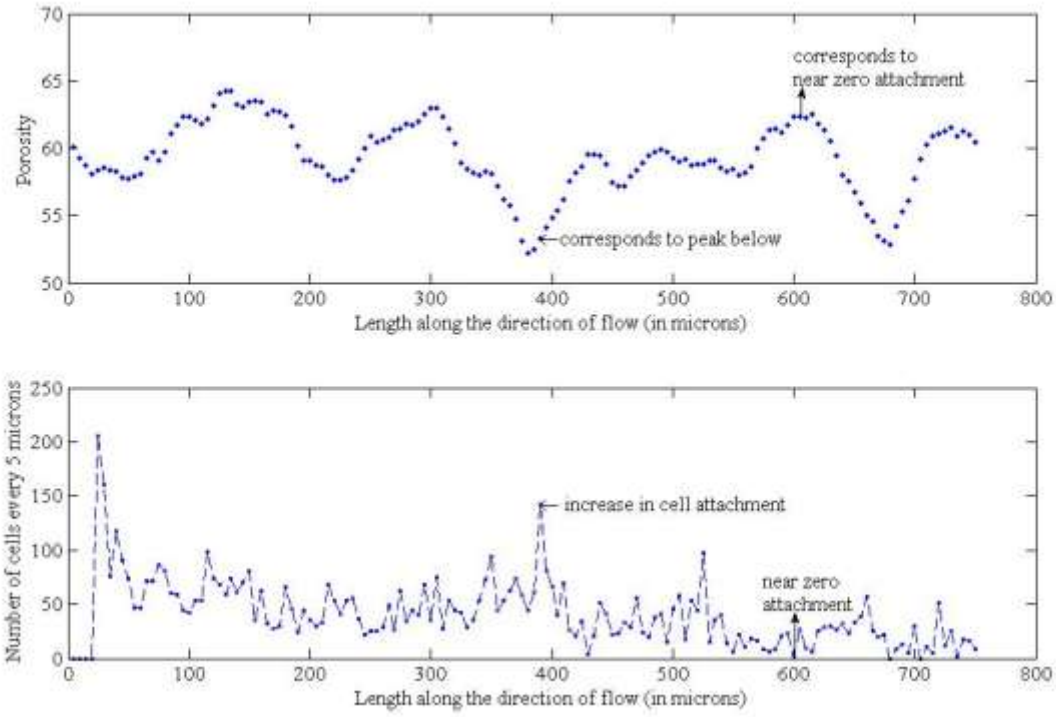

Figure 13: Comparing porosity with cell attachment frequency (a) Porosity along the direction of flow (b) Cell attachment frequency along the direction of flow.

Figure 13 (a) is obtained by plotting the porosity (as obtained by voxel count) at every thin section (slice from the XMCT image) of the scaffold cutout against the length of the cutout in the direction of flow. Figure 13 (b) is obtained by plotting the number of cells attached at each thin section of the scaffold (number of cells attached at a slice is counted) against the length of the cutout in the direction of flow. Figure 13 shows the irregular pattern of cell attachment in a scaffold. We can see from Figure 13 (b) that a small number of slices have a much higher attachment compared to the others. A significant peak in attachment in Figure 13 (b) corresponds to a section that corresponds to a sharp dip in porosity. A dip in cell attachment at the section at 600 micron from the inlet in Figure 13 (b) corresponds to high porosity as seen in Figure 13 (a). But a similar section with a sharp dip in porosity 680 micron from the inlet does not show a similar peak in the attachment. This comparison suggests that although there seems to be a link

between converging-diverging channels in the scaffold to cell attachment pattern, the behavior cannot be described as purely a porosity based phenomenon. However, this behavior does indicate a need to investigate the regions that show a high level of attachment.

To better understand what is happening inside the scaffold, visualization of streamlines and attachment pattern in the scaffold was done using Avizo software to obtain Figure 13.

From Figures 4, 5 and 14 we can see that attachment occurs where diffusion is much greater than convection. No attachment is seen in regions where the component of velocity at the center of the particle normal to the surface points away from the surface.

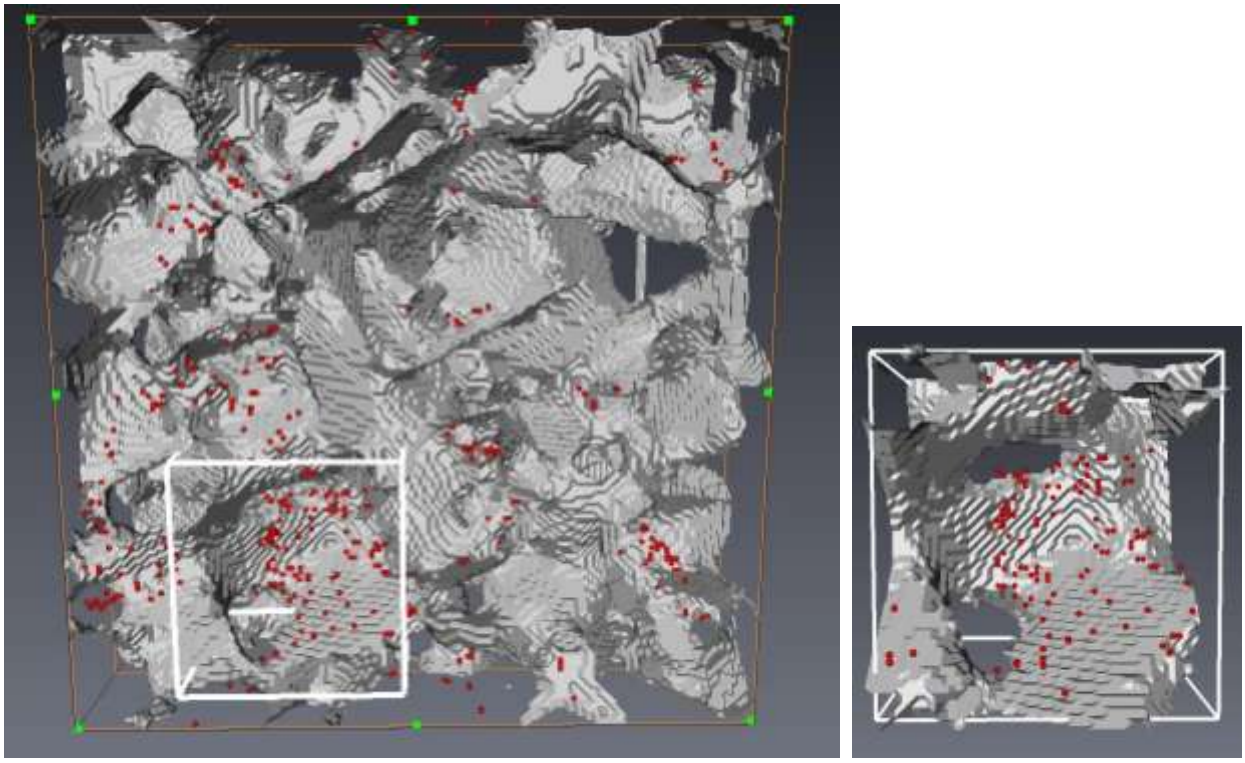

(a) (b)

Figure 14: Visualization of attachment pattern in a scaffold (a) Attachment pattern in a section inside the scaffold (b) pore of interest (c) Pore with attachment points; front view, 90 degree rotated, back view (d) Pore with streamlines; front view, 90 degree rotated, back view (e) Streamlines with attachment points; front view, 90 degree rotated, back view (f) Pore with attachment points and streamlines; front view, 90 degree rotated, back view. (Figure continued)

(Figure 14 continued)

(c)

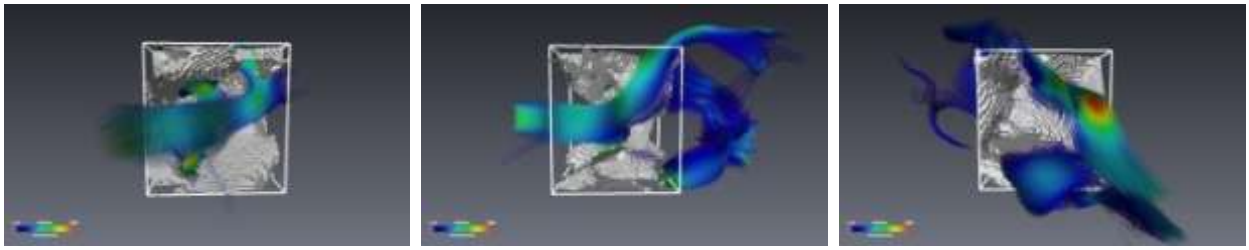

(d)

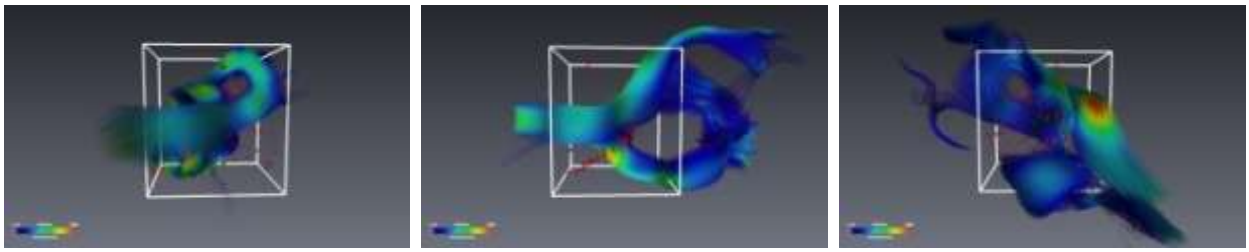

(e)

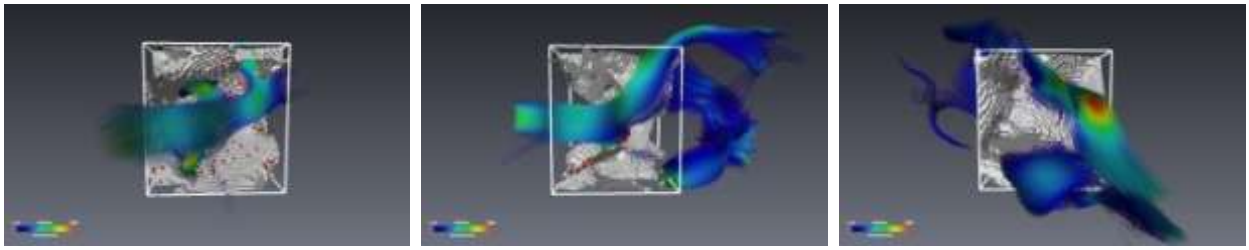

(f)

CHAPTER 5 CONCLUSIONS AND FUTURE WORK

5.1 Conclusions

A model to track particles flowing through a porous media in a Stokes flow regime (Creeping flow) has applications ranging from biomedical, microfluidics, environmental and water treatment. A particularly important application of this research would be in predicting likely cell attachment patterns in disordered polymeric scaffolds, which is a first step in many modern tissue engineering processes. Currently available models for particle transport in a porous media have a limitation in that they do not incorporate the real internal structure of the porous media. Hence, models tend to be more qualitative than quantitative.

We developed an image-based model that takes into account the complex internal microstructure of a real porous material, by incorporating the sample XMCT image into the simulation. We can understand how particles move and where they are likely to attach inside a disordered porous media at creeping flow conditions using this simulation. We assume that the suspension of particles in the medium is dilute, so that the simulation can simplify the process to sending in particles from the porous material inlet one after the other sequentially. Particle motion inside the porous material is controlled by a deterministic convection component, a stochastic diffusion component and an electrostatic component. Convective forces are calculated using the velocity profile inside the porous material, obtained by numerically solving the Stokes flow using FEM. Diffusion is modeled by a random walk process. Electrostatic forces (Van der waals force and Electrostatic double layer force) are estimated using analytical expressions for the interaction of a colloid particle with a surface. In the model the condition for attachment is

that the sum of the components of the convective and electrostatic forces acting at the center of the particle should be pointing into the pore surface.

We have demonstrated that the image based computational model developed in this thesis, can be effectively used to study the effect of flow characteristics on particle movement and the likely sites of particle attachment. Flow characteristics are in turn dependent on the material internal geometry, fluid properties such as viscosity and the pressure gradient applied at the inlet and outlet. The model is set up to study the effect of the magnitude and type of surface charges on the pore surface, on the particle attachment pattern. While we recognize that this is a simplified model, it is an important first step in obtaining quantitative data for the behavior in real materials.

Tissue engineered material created by seeding bone precursor cells onto a porous degradable scaffold is considered the future of bone repair. A major obstacle to achieving this goal is the difficulty in making uniformly seeded scaffolds. The image based model for particle transport and attachment in a disordered porous material developed during this research can be used to study the effect of scaffold internal structure and resulting flow characteristics on the cell seeding pattern in a scaffold. A real disordered scaffold material was created from Polyethylene glycol using salt leaching method and the simulation was performed on an XMCT image of the sample.

The simulation was run at different Peclet numbers, but all for the Stokes flow regime. Cell attachment in the scaffold was found to be concentrated at the region near the inlet for low Peclet numbers. More cells travelled further along the scaffold in the direction of flow at higher Peclet numbers resulting in a more even pattern of cell attachment. But even at very high Peclet numbers clustering of attachment at some spots was observed. This behavior is attributed to the combination of local pore geometry and local hydrodynamics. Visualization of the preliminary

data suggests that the scaffold has small pores carrying flow at high velocity leading to much larger pores causing the velocity of the medium to decrease sharply creating low velocity zones where the diffusion is stronger than convection resulting in a much higher attachment of cells at these locations.

Despite the evidence provided in the current work, more direct evidence is necessary to pin particle attachment pattern to specific artifacts of material internal structure. Obtaining information about pore shape and pore size distribution for the porous material will provide a direct link between the observed attachment pattern and pore characteristics.

Pumping the fluid into the scaffold in pulses (oscillatory perfusion flow) could result in a more uniform particle attachment pattern. A sufficiently high velocity pulse would force the particles deep into the porous material. The time in between pulses would allow diffusion to help create a more uniform attachment-pattern. To test the effect of such a flow pattern on the deposition pattern, it is necessary to incorporate changes in the pore space velocity profile with time into the model.

The shape of the internal pore space would change if particle attachment clusters at some region with a narrow connection to a nearby pore. The permeability of the porous material (scaffold) would change with particle attachment. Recomputing the velocity profile for the changed internal pore structure after a set number of iterations would prevent inaccuracies resulting from ignoring changes to velocity profile in the porous media with time.

REFERENCES

Agrawal, C. M. and R. B. Ray (2001). "Biodegradable polymeric scaffolds for musculoskeletal tissue engineering." Journal of Biomedical Materials Research **55**(2): 141-150.

Alvarez-Barreto, J. F., S. M. Linehan, et al. (2007). "Flow perfusion improves seeding of tissue engineering scaffolds with different architectures." Annals of Biomedical Engineering **35**(3): 429-442.

Bear, J. (1972). Dynamics of Fluids in Porous Media. New York, American Elsevier Pub. Co.

Bhattad, P., C. S. Willson, et al. (2010). Segmentation of Low-contrast Three-phase X-ray Computed Tomography Images of Porous Media. Advances in Computed Tomography for Geomaterials, GeoX 2010. A. H. R. Khalid A. Alshibli. New Orleans, LA., ISTE Ltd. and John Wiley & Sons, Inc.

Bok, M., H. Y. Li, et al. (2009). "The Dynamics of Surface Acoustic Wave-Driven Scaffold Cell Seeding." Biotechnology and Bioengineering **103**(2): 387-401.

Botchwey, E. A., M. A. Dupree, et al. (2003). "Tissue engineered bone: Measurement of nutrient transport in three-dimensional matrices." Journal of Biomedical Materials Research Part A **67A**(1): 357-367.

Botchwey, E. A., S. R. Pollack, et al. (2001). "Bone tissue engineering in a rotating bioreactor using a microcarrier matrix system." Journal of Biomedical Materials Research **55**(2): 242-253.

Cancedda, R., P. Giannoni, et al. (2007). "A tissue engineering approach to bone repair in large animal models and in clinical practice." Biomaterials **28**(29): 4240-4250.

Datta, A. (2007). Characterization of Polyethylene Glycol Hydrogels for Biomedical Applications. Chemical Engineering. Baton Rouge, Louisiana State University. **Master of Science in Chemical Engineering**.

Deville, S., E. Saiz, et al. (2006). "Freeze casting of hydroxyapatite scaffolds for bone tissue engineering." Biomaterials **27**(32): 5480-5489.

Du, D. J., K. Furukawa, et al. (2008). "Oscillatory perfusion seeding and culturing of osteoblast-like cells on porous beta-tricalcium phosphate scaffolds." Journal of Biomedical Materials Research Part A **86A**(3): 796-803.

Freed, L. E., A. P. Hollander, et al. (1998). "Chondrogenesis in a cell-polymer-bioreactor system." Experimental Cell Research **240**(1): 58-65.

Freed, L. E. and G. Vunjak-Novakovic, Eds. (2000). Principles of tissue engineering. New York, Academic Press

Gomes, M. E., V. I. Sikavitsas, et al. (2003). "Effect of flow perfusion on the osteogenic differentiation of bone marrow stromal cells cultured on starch-based three-dimensional scaffolds." Journal of Biomedical Materials Research Part A **67A**(1): 87-95.

Habibovic, P. and K. de Groot (2007). "Osteoinductive biomaterials - properties and relevance in bone repair." Journal of Tissue Engineering and Regenerative Medicine **1**(1): 25-32.

Holy, C. E., M. S. Shoichet, et al. (2000). "Engineering three-dimensional bone tissue in vitro using biodegradable scaffolds: Investigating initial cell-seeding density and culture period." Journal of Biomedical Materials Research **51**(3): 376-382.

Huebner, K. H., E. A. Thornton, et al. (1995). The Finite Element Method for Engineers, John Wiley & Sons, Inc.

Ishaug-Riley, S. L., G. M. Crane-Kruger, et al. (1998). "Three-dimensional culture of rat calvarial osteoblasts in porous biodegradable polymers." Biomaterials **19**(15): 1405-1412.

Jones, J. R., O. Tsigkou, et al. (2007). "Extracellular matrix formation and mineralization on a phosphate-free porous bioactive glass scaffold using primary human osteoblast (HOB) cells." Biomaterials **28**(9): 1653-1663.

Kannan, S., A. Balamurugan, et al. (2005). "Electrochemical characterization of hydroxyapatite coatings on HNO3 passivated 316L SS for implant applications." Electrochimica Acta **50**(10): 2065-2072.

Khurana, J. S. (2009). Bone pathology. J. S. Khurana. New York, Humana Press.

Kim, B. S., A. J. Putnam, et al. (1998). "Optimizing seeding and culture methods to engineer smooth muscle tissue on biodegradable polymer matrices." Biotechnology and Bioengineering **57**(1): 46-54.

Lane, N. and K. E. Thompson (2010). Image-Based Pore-Scale Modeling Using the Finite Element Method. Advances in Computed Tomography for Geomaterials GeoX 2010. A. H. R. Khalid A. Alshibli. New Orleans, LA, ISTE Ltd and John Wiley & Sons, Inc.

Long, W., H. O. Huang, et al. (2010). "Pore-scale study of the collector efficiency of nanoparticles in packings of nonspherical collectors." Colloids and Surfaces a-Physicochemical and Engineering Aspects **358**(1-3): 163-171.

Marler, J. J., J. Upton, et al. (1998). "Transplantation of cells in matrices for tissue regeneration." Advanced Drug Delivery Reviews **33**(1-2): 165-182.

Martin, I., D. Wendt, et al. (2004). "The role of bioreactors in tissue engineering." Trends in Biotechnology **22**(2): 80-86.

Nishiguchi, S., S. Fujibayashi, et al. (2003). "Biology of alkali- and heat-treated titanium implants." Journal of Biomedical Materials Research Part A **67A**(1): 26-35.

O'Brien, F. J., B. A. Harley, et al. (2005). "The effect of pore size on cell adhesion in collagen-GAG scaffolds." Biomaterials **26**(4): 433-441.

Oh, W. and W. B. Lindquist (1999). "Image thresholding by indicator kriging." Ieee Transactions on Pattern Analysis and Machine Intelligence **21**(7): 590-602.

Otsuki, B., M. Takemoto, et al. (2006). "Pore throat size and connectivity determine bone and tissue ingrowth into porous implants: Three-dimensional micro-CT based structural analyses of porous bioactive titanium implants." Biomaterials **27**(35): 5892-5900.

Palecek, S. P., J. C. Loftus, et al. (1997). "Integrin-ligand binding properties govern cell migration speed through cell-substratum adhesiveness." Nature **385**(6616): 537-540.

Pietrzak, W. S. (2008). Musculoskeletal Tissue Regeneration : Biological Materials and Methods. Totowa, NJ Humana Press, a part of Springer Science+Business Media, LLC.

Rege, S. D. and H. S. Fogler (1988). "A Network Model for Deep Bed Filtration of Solid Particles and Emulsion Drops." Aiche Journal **34**(11): 1761-1772.

Rose, F. R., L. A. Cyster, et al. (2004). "In vitro assessment of cell penetration into porous hydroxyapatite scaffolds with a central aligned channel." Biomaterials **25**(24): 5507-5514.

Ryan, G., A. Pandit, et al. (2006). "Fabrication methods of porous metals for use in orthopaedic applications." Biomaterials **27**(13): 2651-2670.

Sargeant, A. and T. Goswami (2006). "Hip implants: Paper V. Physiological effects." Materials & Design **27**(4): 287-307.

Shanbhag, S., S. P. Wang, et al. (2005). "Cell distribution profiles in three-dimensional scaffolds with inverted-colloidal-crystal geometry: Modeling and experimental investigations." Small **1**(12): 1208-1214.

Shin, H., S. Jo, et al. (2003). "Biomimetic materials for tissue engineering." Biomaterials **24**(24): 4353-4364.

Sikavitsas, V. I., G. N. Bancroft, et al. (2002). "Formation of three-dimensional cell/polymer constructs for bone tissue engineering in a spinner flask and a rotating wall vessel bioreactor." Journal of Biomedical Materials Research **62**(1): 136-148.

Sikavitsas, V. I., J. S. Temenoff, et al. (2001). "Biomaterials and bone mechanotransduction." Biomaterials **22**(19): 2581-2593.

Vacanti, J. P. (1988). "Beyond Transplantation - 3rd Annual Mixter,Samuel,Jason, Lecture." Archives of Surgery **123**(5): 545-549.

VanGordon, S. B., R. S. Voronov, et al. (2010). "Effects of Scaffold Architecture on Preosteoblastic Cultures under Continuous Fluid Shear." Industrial & Engineering Chemistry Research.

Vunjak-Novakovic, G., B. Obradovic, et al. (1998). "Dynamic cell seeding of polymer scaffolds for cartilage tissue engineering." Biotechnology Progress **14**(2): 193-202.

Weickert, J. and H. Scharr (2002). "A scheme for coherence-enhancing diffusion filtering with optimized rotation invariance." Journal of Visual Communication and Image Representation **13**(1-2): 103-118.

Weinand, C., J. W. Xu, et al. (2009). "Conditions Affecting Cell Seeding Onto Three-Dimensional Scaffolds for Cellular-Based Biodegradable Implants." Journal of Biomedical Materials Research Part B-Applied Biomaterials **91B**(1): 80-87.

Wendt, D., A. Marsano, et al. (2003). "Oscillating perfusion of cell suspensions through three-dimensional scaffolds enhances cell seeding efficiency and uniformity." Biotechnology and Bioengineering **84**(2): 205-214.

Zhao, J., X. Lu, et al. (2008). "Macroporous Ti-based composite scaffold prepared by polymer impregnating method with calcium phosphate coatings." Materials Letters **62**(17-18): 2921-2924.

Zypman, F. R. (2006). "Exact expressions for colloidal plane-particle interaction forces and energies with applications to atomic force microscopy." Journal of Physics-Condensed Matter **18**(10): 2795-2803.

VITA

Tejaswini Narayana was born in 1983 in India. She received her Bachelor of Technology in Chemical Engineering degree from T.K.M College of Engineering, University of Kerala in 2005. She enrolled in the graduate program at LSU in Fall 2008. She will be graduating in May, 2011, with a Master of Science in Chemical Engineering degree.